LETTERS
PUBLISHED ONLINE: 14 MARCH 2016 | DOI: 10.1038/NPHOTON.2016.36
nature photonics

Broadband dispersion-engineered microresonator on a chip

Ki Youl Yang[1], Katja Beha[2], Daniel C. Cole[2], Xu Yi[1], Pascal Del'Haye[2], Hansuek Lee[1], Jiang Li[1], Dong Yoon Oh[1], Scott A. Diddams[2], Scott B. Papp[2] and Kerry J. Vahala[1]*

The control of dispersion in fibre optical waveguides is of critical importance to optical fibre communications systems[1,2] and more recently for continuum generation from the ultraviolet to the mid-infrared[3–5]. The wavelength at which the group velocity dispersion crosses zero can be set by varying the fibre core diameter or index step[2,6–8]. Moreover, sophisticated methods to manipulate higher-order dispersion so as to shape and even flatten the dispersion over wide bandwidths are possible using multi-cladding fibres[9–11]. Here we introduce design and fabrication techniques that allow analogous dispersion control in chip-integrated optical microresonators, and thereby demonstrate higher-order, wide-bandwidth dispersion control over an octave of spectrum. Importantly, the fabrication method we employ for dispersion control simultaneously permits optical Q factors above 100 million, which is critical for the efficient operation of nonlinear optical oscillators. Dispersion control in high-Q systems has become of great importance in recent years with increased interest in chip-integrable optical frequency combs[12–32].

High-Q microresonators, through the cavity enhancement of an input field, enable many important optical devices and functions[33]. These applications include frequency comb generation, pulse sources, cascaded Raman lasers, stimulated Brillouin lasers and harmonic generation[12–39]. In many systems the control of modal dispersion is helpful or essential. This is particularly important in parametric oscillators[40,41] where the local dispersion must be anomalous and in frequency microcombs where both the sign of the dispersion as well as its spectral shape are critical for comb operation[12,14]. The spectral bandwidth and coherent operation are strongly influenced by dispersion and there has been remarkable progress in these areas, including sub-comb synchronization[21–24], soliton generation[25–31] and dispersive wave formation[18,19,27].

There have been multiple approaches to engineering dispersion in microresonators. The control of the waveguide width and height in Si_3N_4, diamond, MgF_2 and CaF_2 resonators alters the geometric dispersion[16,32,42,43]. HfO_2-coated Si_3N_4 and oxidized Si resonators also provide dispersion control[44,45].

This Letter studies dispersion control in ultrahigh-Q silica disks using a method that is inspired by dispersion engineering in optical fibres. By creating multi-wedge disks and precisely controlling their geometry during microfabrication, we have devised a technique that lithographically controls higher-order dispersion over an octave of bandwidth. After introducing the approach and microfabrication method, resonator dispersion is measured at various bands from 960 to 2,100 nm and compared with modelling to confirm dispersion control.

Optical fibre designers use multiple cladding layers to control the magnitude, sign and spectral profile of the combined material and waveguide dispersion[2,10]. We devised a method for dispersion control in disk resonators that is analogous to these methods. Fig. 1a compares the dispersion of a single-wedge disk with that of a single-core optical fibre. Details of the fabrication and basic properties of the single-wedge disk are contained in ref. 37. Briefly, the device is fabricated from thermal silica on silicon using lithography combined with wet and dry etching. In terms of dispersion control, the wedge angle θ is a key parameter. The group index spectra of three resonators that differ only in their wedge angles are shown in Fig. 1a. The group index of bulk silica is also provided for comparison. In effect, the wedge angle introduces a component of normal dispersion that is stronger for smaller wedge angles[37,46]. By comparison, in the single-clad fibre[8], the group index is varied (for a fixed core diameter) through control of Δn.

Figure 1b shows the calculated optical mode in the single-wedge disk and the optical fibre to further understand the mechanism of dispersion control in each system. In the resonator, longer-wavelength modes see their centroid of motion around the resonator shift inwards (that is, smaller radii) so that the effective optical path is smaller. This is equivalent to normal dispersion[37,46]. In the fibre, longer-wavelength modes have a greater spatial overlap with the lower-index cladding. Greater contrast between the core and cladding indices therefore strengthens this normal contribution to dispersion.

This similarity between the resonator and fibre cases suggests a method to engineer dispersion in the resonator that is illustrated in Fig. 1c for fundamental modes in the resonator and fibre. In the right-hand panel, the case of a multi-clad fibre is considered in relation to a resonator featuring several wedge angles. The multi-clad fibre can be understood by analysing the dispersion in short- and long-wavelength cases[10]. Short-wavelength modes are confined primarily by the core region and experience a group index that is similar to a corresponding single-core fibre. Longer-wavelength modes are primarily confined by the secondary cladding layer. The corresponding spectral dependence of the group index can be understood as a transition between these two extreme cases (see the spectrum for a multi-clad fibre in Fig. 1c). The wavelength at which the transition occurs can be correspondingly engineered[9,11]. For example, by placing the outer, higher-index region closer to the inner core, the transition will occur at shorter wavelengths.

Using analogous reasoning for the resonator, the case of a double-wedge resonator is considered in the left-hand panel of Fig. 1c. In this case, the shorter-wavelength modes experience the outer, larger-angle wedge ($\theta_1 = 45°$) whereas the longer-wavelength modes experience the inner, smaller wedge angle ($\theta_2 = 10°$). The spectral dependence of the group index thereby transitions between these two extreme cases. By controlling the specific wedge angles the

[1]T. J. Watson Laboratory of Applied Physics, California Institute of Technology, Pasadena, California 91125, USA. [2]Time and Frequency Division, National Institute of Standards and Technology, Boulder, Colorado 80305, USA. *e-mail: vahala@caltech.edu

© 2016 Macmillan Publishers Limited. All rights reserved

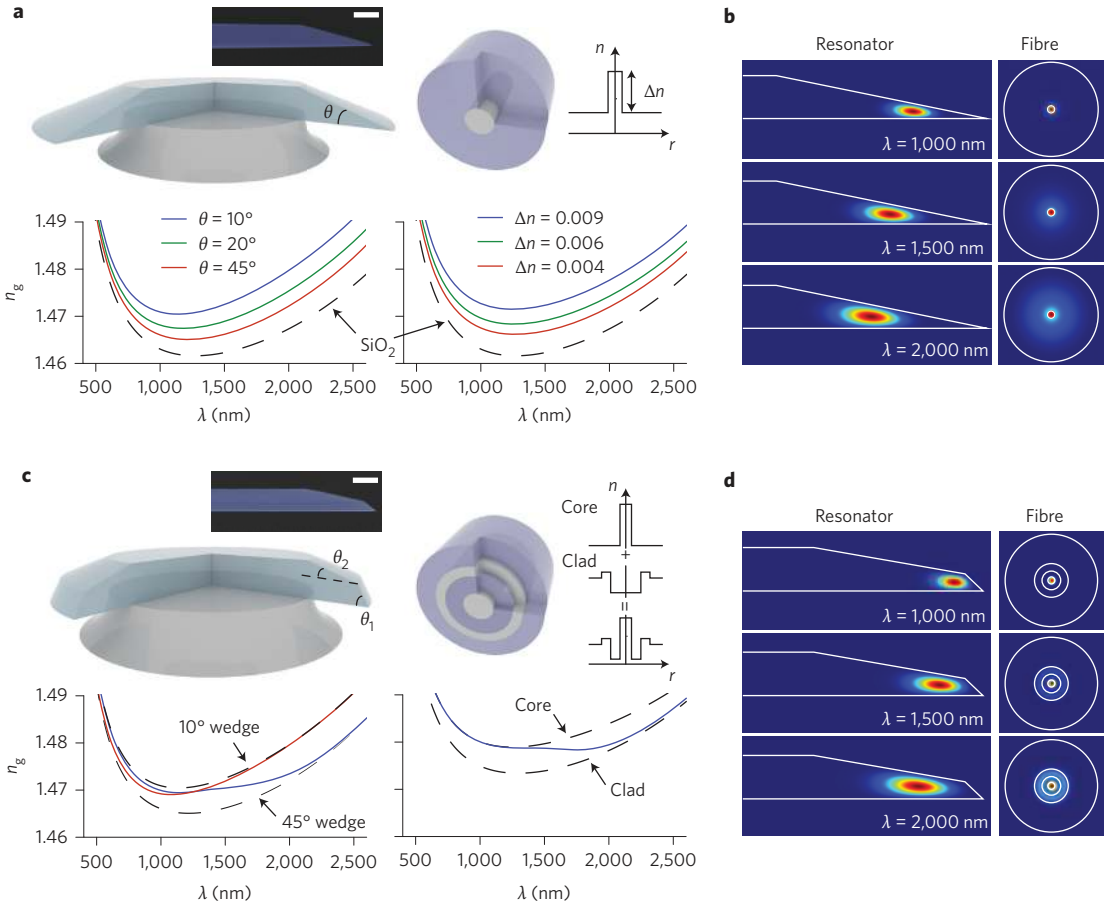

Figure 1 | Fibre-inspired cavity dispersion design. a, The upper diagrams depict a single-wedge resonator (left) and a single-core fibre (right); and lower panels give the corresponding group-index (n_g) spectra of the fundamental modes (θ is the wedge angle of the resonator and Δn is the core-cladding refractive index difference). The dashed curves give the bulk group index of silica. Calculations assume a resonator diameter of 3 mm and a fibre core diameter of 11 μm. The HE_{11} mode (fundamental) is calculated for the optical fibre. A micrograph of the resonator cross-section (scale bar = 10 μm) and the fibre refractive index profile are provided as insets. **b**, Finite element simulation of the fundamental mode in a single-wedge disk (left panel) and single-clad fibre (right panel) at wavelengths of 1,000 nm, 1,500 nm and 2,000 nm. The index contrast and core diameter in the fibre mode calculation have been set to $\Delta n = 0.0028$ μm and 4.5 μm to make the variation in the mode profile with wavelength more easily observable. **c**, As in **a**, but for a double-wedge disk and a multi-clad fibre. The dashed lines in the group index spectra give either the single-wedge results (10° and 45° cases) or the single-core and clad cases for the fibre. The blue curve in the lower right panel gives the multi-clad fibre case. The blue and red curves in the lower left panel indicate the multi-wedge resonator where the angle ordering is red (45° (outer) → 10° (inner)) and blue (10° (outer) → 45° (inner)). **d**, Same as **b**, but for a double-wedge resonator and a multi-clad fibre. The core diameter in the multi-clad fibre plots is set to 4.5 μm to make the variation in the mode profile with wavelength more easily observable.

long- and short-wavelength limiting behaviour is controlled. Likewise, in analogy with the multi-clad fibre, the location of the wedge-angle transition allows control of the wavelength band over which the group index transitions between these two limits. As shown below, this concept can be extended to the design of the group index of a quadruple-wedge disk, which provides more flexibility in dispersion control over a wider range of wavelengths.

The process for producing multi-wedge disks is an extension of the techniques developed for the original single-wedge disk resonator[37]. Fabrication begins with thermally grown SiO_2 on Si, which is then processed with photolithography and wet etching into single-wedge shaped disks (see the top row in Fig. 2a) in which the wedge angle can be controlled from 8° to 55°. A double wedge (see the lower row in Fig. 2a) is created through another cycle of thermal oxidation, photolithography and wet etching. During this second cycle, the angle of the extra wedge is adjusted as before and its height is controlled by the duration of the etching. Calibrations have shown that the height increases at a rate of ~10 nm min^{-1} (see Fig. 2b), resulting in the following spectral rates: free-spectral-range (FSR) ~ 400 kHz min^{-1} and D_2 (= ΔFSR per mode) ~300 Hz min^{-1} (see Fig. 2d). The process can be repeated to add extra wedges. A four-wedge structure is shown in Fig. 2f. The process achieved Q factors of 1.6×10^8, 1.1×10^8 and 1.6×10^8 for single-, double-, and quadruple-wedge disks, respectively (see Fig. 2c).

To characterize dispersion in the resonator we measure FSR_μ (μ is mode index) in several wavelength bands using a method described below, and calculate $D_2(\mu)$, the ΔFSR per mode at mode μ, which is related to the group velocity dispersion through the following expression[13,44–46]:

$$\beta_2(\mu) = \left.\frac{\partial^2 \beta}{\partial \omega^2}\right|_{\omega=\omega_\mu} \approx -\frac{1}{4\pi^2 R}\frac{D_2(\mu)}{\mathrm{FSR}_\mu^3} \quad (1)$$

where β is the mode propagation constant at the angular frequency ω, and R is the resonator radius. As a preliminary test of dispersion control in a multi-wedge resonator, double-wedge disks were fabricated with a series of outer wedge heights (t, inset in Fig. 2d). A plot of the measured D_2 (at 1,550 nm) versus t is provided in Fig. 2d, and the solid line is calculated using a finite element solver. D_2 increases with t at the average rate of 30 Hz nm^{-1}. The error between the measured D_2 and a predicted D_2 (using the SEM measurements

© 2016 Macmillan Publishers Limited. All rights reserved

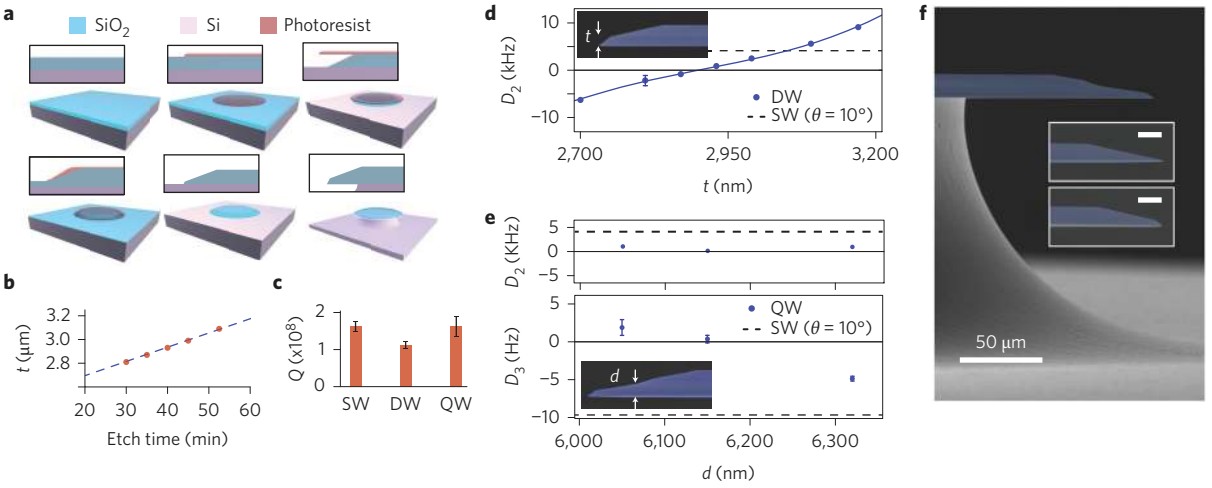

Figure 2 | Microfabrication process flow and side-view micrographs. a, The flow steps required to fabricate a double-wedge resonator. **b**, Measured wedge height (*t*, see inset of **d**) control as a function of etch time. **c**, Measured *Q* factor of the transverse magnetic (TM) fundamental mode in single-, double- and quadruple-wedge disks. **d**, D_2 (= ΔFSR per mode) as a function of *t* for a double-wedge disk measured at 1,550 nm. **e**, D_3 and D_2 as a function of the third wedge height (*d*, see inset) of a quadruple-wedge disk measured at 1,550 nm. **f**, Scanning electron micrographs showing the profile of a quadruple-wedge resonator. Inset, profiles for single- (top, scale bar = 10 μm) and double-wedge resonators (bottom, scale bar = 10 μm).

input to finite-element simulation) had a standard deviation of 500 Hz.

In addition, quadruple-wedge disks were fabricated with a variable geometric parameter *d* (see inset in Fig. 2e). Figure 2e shows measurements of D_2 and D_3 (at 1,550 nm) in such a structure plotted versus *d*. Here, we define dispersion coefficients as

$$f_\mu = f_0 + D_1\mu + \frac{D_2}{2!}\mu^2 + \frac{D_3}{3!}\mu^3 + \cdots \quad (2)$$

where f_μ is the frequency of the mode with index μ ($\mu = 0$ corresponds to the mode at which the dispersion is measured) and D_1, D_2, D_3 correspond to FSR, ΔFSR per mode and the third-order dispersion parameters[24–27]. The third wedge in the quadruple wedge structure introduces an additional component of geometric dispersion so that both *t* and *d* can be varied for dispersion control. Nonetheless, variations in microfabrication will cause corresponding variations in the fabricated resonator dispersion (Supplementary Section II).

To measure the FSR quickly and over a broad range of wavelengths, we have modified a method reported in ref. 46. The measurement set-up is shown in Fig. 3a and incorporates a frequency comb generated using electro-optical modulation (EOM) in conjunction with optical broadening using a high-nonlinearity fibre (HNLF). The seed laser for the EOM comb was a tunable laser that was scanned continuously during the measurement. Further details on this EOM comb are provided in ref. 48. The comb bandwidth was approximately 300 nm centred around 1,550 nm and the line spacing (equal to the drive frequency f_{eo}) was tunable and set to coincide approximately with the resonator FSR of ~22 GHz. A relatively narrow band of comb frequencies was coupled to the resonator using a tunable optical filter and the transmitted optical signals were measured using a photodetector. A measurement proceeded by first setting the tunable filter to a desired wavelength. The optical filter had a 3-dB bandwidth of 3 nm, so approximately 15 comb teeth (comb spacing ~22 GHz) would be launched to the resonator input port. The photodetected signal was then observed as a time trace on an oscilloscope that was synchronized with the scanning seed laser. If the microwave frequency used to establish the EOM comb line spacing was set to exactly coincide with the FSR of the resonator at the selected wavelength, then a single transmission minimum would appear as the filtered comb teeth are all coupled to the neighbouring resonances of the resonator. By slightly tuning the comb drive frequency away from the FSR value, the single transmission minimum would break up into many separate peaks as the comb teeth would now achieve resonance at slightly different points in the laser scan. The resolution in determination of the FSR by this method was estimated to be about 100 kHz. It is also important to note that the method provides an FSR value that is spectrally averaged as multiple comb teeth participate in the process. This fact tends to smooth the data with respect to effects such as avoided-crossings of mode families. In addition to measurements in the 1,500 nm band, the EOM comb was also shifted in wavelength to 2,100 nm by difference frequency generation using a 895 nm pump laser. Measurements of FSR using the technique reported in ref. 46 were conducted at 980 and 1,300 nm. Collectively, these measurements provided a very good picture of how dispersion could be modified through judicious cavity design.

Figure 3b–d shows measured FSR, D_2 and the results of simulations for the device structures provided in the insets. As has been noted in ref. 46, a single wedge contributes geometrical dispersion that is both normal and approximately spectrally flat. Also, smaller wedge angles increase the strength of this contribution. In Fig. 3b, the zero dispersion wavelength (λ_{ZDW}), has been shifted by this effect to 1.5 μm (refs 37,46) (material dispersion has a λ_{ZDW} near 1.3 μm)[47].

In the double-wedge resonator (Fig. 3c) there is a gradual onset of the geometrical dispersion from shorter to longer wavelengths as a result of a steep outer wedge (low normal dispersion) to the shallow interior wedge (larger normal dispersion). The overall effect is to provide a flattening of the dependence of FSR on wavelength over a broad range of wavelengths. The dispersion in the transition is therefore reduced. The addition of further wedges can be used to extend this control to longer wavelengths. In the quadruple-wedge design the third wedge provides control out to 2,000 nm (Fig. 3d).

This study has proposed and tested a resonator dispersion control approach that is inspired by dispersion control methods in multi-cladding optical fibres. This approach provides the first method of controlling resonator dispersion over a broad range of wavelengths (equivalent to having control over high-order dispersion).

© 2016 Macmillan Publishers Limited. All rights reserved

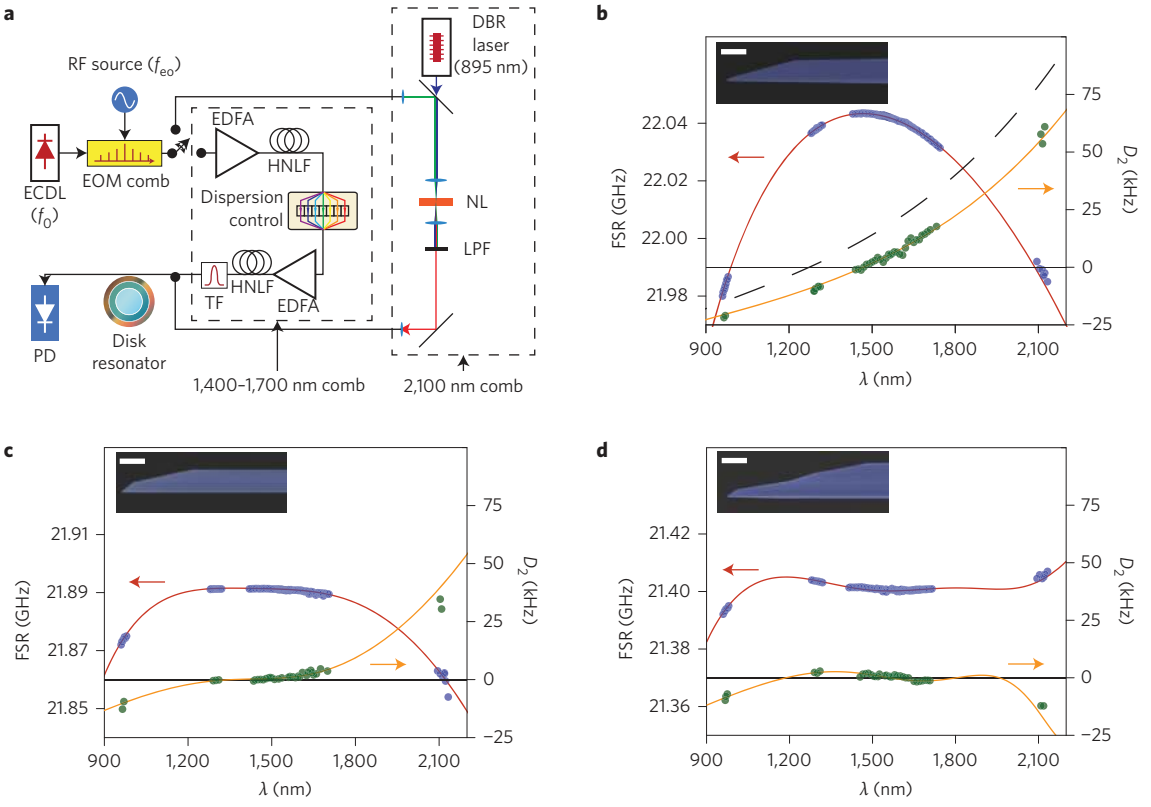

Figure 3 | Dispersion characterization. a, FSR measurement set-up for 1,400–1,700 nm and 2,100 nm bands. The 2,100 nm band comb was generated as the difference in frequency between an 895 nm distributed Bragg reflector (DBR) laser and a 1,550 nm EOM comb modulated at the frequency f_{eo}. ECDL, external cavity diode laser; EDFA, erbium doped fibre amplifier; TF, tunable bandpass filter; NL, nonlinear crystal; LPF, lowpass optical filter; PD, photodetector. **b**, FSR and D_2 for single-wedge disk. Blue and green data points are measured FSR and D_2, respectively; red and orange lines are numerical results. The cavity geometry is imported from SEM (inset, scale bar = 10 μm) and AFM images for finite element simulations. **c**,**d**, As in panel **b**, but for double (**c**) and quadruple (**d**) wedges.

The approach builds on high-Q silica-on-silicon wedge resonator fabrication by adding extra wedge angles to the resonator. The position of each wedge and its angle determine the wavelength location and strength of a corresponding contribution to geometric dispersion. As a result, the approach is highly intuitive and when combined with numerical modelling provides a highly controllable way to engineer dispersion over broad wavelength bands. Dispersion engineered high-Q resonators, as described here, will be useful in nonlinear resonator devices such as frequency microcombs. Moreover, the methods can also be applied in the control of dispersion in nonlinear waveguide structures.

Methods

Methods and any associated references are available in the online version of the paper.

Received 17 May 2015; accepted 4 February 2016; published online 14 March 2016

References

1. Agrawal, G. P. *Nonlinear Fiber Optics* (Academic, 2007).
2. Ainslie, B. J. & Day, C. R. A review of single-mode fibers with modified dispersion characteristics. *J. Lightwave Technol.* **4,** 967–979 (1986).
3. Ranka, J. K., Windeler, R. S. & Stentz, A. J. Visible continuum generation in air-silica microstructure optical fibers with anomalous dispersion at 800 nm. *Opt. Lett.* **25,** 25–27 (2000).
4. Dudley, J. M., Genty, G. & Coen, S. Supercontinuum generation in photonic crystal fiber. *Rev. Mod. Phys.* **78,** 1135–1184 (2006).
5. Petersen, C. R. *et al.* Mid-infrared supercontinuum covering the 1.4–13.3 μm molecular fingerprint region using ultra-high NA chalcogenide step-index fibre. *Nature Photon.* **8,** 830–834 (2014).
6. Cohen, L., Lin, C. & French, W. Tailoring zero chromatic dispersion into the 1.5–1.6 μm low-loss spectral region of single-mode fibres. *Electron. Lett.* **15,** 334–335 (1979).
7. White, K. & Nelson, B. Zero total dispersion in step-index monomode fibres at 1.30 and 1.55 μm. *Electron. Lett.* **15,** 396–397 (1979).
8. Tsuchiya, H. & Imoto, N. Dispersion-free single-mode fibre in 1.5 μm wavelength region. *Electron. Lett.* **15,** 476–478 (1979).
9. Kawakami, S. & Nishida, S. Characteristics of a doubly clad optical fiber with a low-index inner cladding. *IEEE J. Quant. Electron.* **10,** 879–887 (1974).
10. Cohen, L., Mammel, W. & Jang, S. Low-loss quadruple-clad single-mode lightguides with dispersion below 2 ps/km-nm over the 1.28–1.65 μm wavelength range. *Electron. Lett.* **18,** 1023–1024 (1982).
11. Etzkorn, H. & Heinlein, W. Low-dispersion single-mode silica fibre with undoped core and three F-doped claddings. *Electron. Lett.* **20,** 423–424 (1984).
12. Del'Haye, P. *et al.* Optical frequency comb generation from a monolithic microresonator. *Nature* **450,** 1214–1217 (2007).
13. Del'Haye, P., Arcizet, O., Gorodetsky, M., Holzwarth, R. & Kippenberg, T. Frequency comb assisted diode laser spectroscopy for measurement of microcavity dispersion. *Nature Photon.* **3,** 529–533 (2009).
14. Kippenberg, T. J., Holzwarth, R. & Diddams, S. A. Microresonator-based optical frequency combs. *Science* **332,** 555–559 (2011).
15. Del'Haye, P. *et al.* Octave spanning tunable frequency comb from a microresonator. *Phys. Rev. Lett.* **107,** 063901 (2011).
16. Okawachi, Y. *et al.* Octave-spanning frequency comb generation in a silicon nitride chip. *Opt. Lett.* **36,** 3398–3400 (2011).
17. Herr, T. *et al.* Universal formation dynamics and noise of Kerr-frequency combs in microresonators. *Nature Photon.* **6,** 480–487 (2012).
18. Lamont, M. R., Okawachi, Y. & Gaeta, A. L. Route to stabilized ultrabroadband microresonator-based frequency combs. *Opt. Lett.* **38,** 3478–3481 (2013).
19. Coen, S., Randle, H. G., Sylvestre, T. & Erkintalo, M. Modeling of octave-spanning Kerr frequency combs using a generalized mean-field lugiato–lefever model. *Opt. Lett.* **38,** 37–39 (2013).
20. Chembo, Y. K. & Menyuk, C. R. Spatiotemporal Lugiato–Lefever formalism for Kerr-comb generation in whispering-gallery-mode resonators. *Phys. Rev. A* **87,** 053852 (2013).

© 2016 Macmillan Publishers Limited. All rights reserved

21. Li, J., Lee, H., Chen, T. & Vahala, K. J. Low-pump-power, low-phase-noise, and microwave to millimeter-wave repetition rate operation in microcombs. *Phys. Rev. Lett.* **109,** 233901 (2012).
22. Del'Haye, P., Beha, K., Papp, S. B. & Diddams, S. A. Self-injection locking and phase-locked states in microresonator-based optical frequency combs. *Phys. Rev. Lett.* **112,** 043905 (2014).
23. Papp, S. B. *et al.* Microresonator frequency comb optical clock. *Optica* **1,** 10–14 (2014).
24. Del'Haye, P. *et al.* Phase steps and resonator detuning measurements in microresonator frequency combs. *Nature Commun.* **6,** 5668 (2015).
25. Herr, T. *et al.* Temporal solitons in optical microresonators. *Nature Photon.* **8,** 145–152 (2014).
26. Herr, T. *et al.* Mode spectrum and temporal soliton formation in optical microresonators. *Phys. Rev. Lett.* **113,** 123901 (2014).
27. Brasch, V. *et al.* Photonic chip–based optical frequency comb using soliton Cherenkov radiation. *Science* **351,** 357–360 (2016).
28. Xue, X. *et al.* Mode-locked dark pulse Kerr combs in normal-dispersion microresonators. *Nature Photon.* **9,** 594–600 (2015).
29. Jost, J. D. *et al.* Counting the cycles of light using a self-referenced optical microresonator. *Optica* **2,** 706–711 (2015).
30. Yi, X., Yang, Q.-F., Yang, K. Y., Suh, M.-G. & Vahala, K. Soliton frequency comb at microwave rates in a high-*Q* silica microresonator. *Optica* **2,** 1078–1085 (2015).
31. Liang, W. *et al.* High spectral purity Kerr frequency comb radio frequency photonic oscillator. *Nature Commun.* **6,** 7957 (2015).
32. Grudinin, I. S. & Yu, N. Dispersion engineering of crystalline resonators via microstructuring. *Optica* **2,** 221–224 (2015).
33. Vahala, K. J. Optical microcavities. *Nature* **424,** 839–846 (2003).
34. Peccianti, M. *et al.* Demonstration of a stable ultrafast laser based on a nonlinear microcavity. *Nature Commun.* **3,** 765 (2012).
35. Spillane, S., Kippenberg, T. & Vahala, K. Ultralow-threshold Raman laser using a spherical dielectric microcavity. *Nature* **415,** 621–623 (2002).
36. Rong, H. *et al.* An all-silicon Raman laser. *Nature* **433,** 292–294 (2005).
37. Lee, H. *et al.* Chemically etched ultrahigh-*Q* resonator on a chip. *Nature Photon.* **6,** 369–373 (2012).
38. Büttner, T. F. *et al.* Phase-locking and pulse generation in multi-frequency Brillouin oscillator via four wave mixing. *Sci. Rep.* **4,** 5032 (2014).
39. Carmon, T. & Vahala, K. J. Visible continuous emission from a silica microphotonic device by third-harmonic generation. *Nature Phys.* **3,** 430–435 (2007).
40. Kippenberg, T., Spillane, S. & Vahala, K. Kerr-nonlinearity optical parametric oscillation in an ultrahigh-*Q* toroid microcavity. *Phys. Rev. Lett.* **93,** 083904 (2004).
41. Grudinin, I. S., Yu, N. & Maleki, L. Generation of optical frequency combs with a CaF_2 resonator. *Opt. Lett.* **34,** 878–880 (2009).
42. Saha, K. *et al.* Broadband parametric frequency comb generation with a 1-μm pump source. *Opt. Express* **20,** 26935–26941 (2012).
43. Hausmann, B., Bulu, I., Venkataraman, V., Deotare, P. & Lončar, M. Diamond nonlinear photonics. *Nature Photon.* **8,** 369–374 (2014).
44. Riemensberger, J. *et al.* Dispersion engineering of thick high-*Q* silicon nitride ring-resonators via atomic layer deposition. *Opt. Express* **20,** 27661–27669 (2012).
45. Jiang, W. C., Zhang, J., Usechak, N. G. & Lin, Q. Dispersion engineering of high-*Q* silicon microresonators via thermal oxidation. *Appl. Phys. Lett.* **105,** 031112 (2014).
46. Li, J., Lee, H., Yang, K. Y. & Vahala, K. J. Sideband spectroscopy and dispersion measurement in microcavities. *Opt. Express* **20,** 26337–26344 (2012).
47. Malitson, I. Interspecimen comparison of the refractive index of fused silica. *J. Opt. Soc. Am.* **55,** 1205–1208 (1965).
48. Beha, K. *et al.* Self-referencing a continuous-wave laser with electro-optic modulation. Preprint at http://arxiv.org/abs/1507.06344 (2015).

Acknowledgements

We gratefully acknowledge support from the Defense Advanced Research Projects Agency under the QuASAR program, the National Institute of Standards and Technology, the Kavli Nanoscience Institute and the Institute for Quantum Information and Matter, an NSF Physics Frontiers Center with support of the Gordon and Betty Moore Foundation. D.C.C. acknowledges support from the NSF GRFP under Grant No. DGE 1144083.

Author contributions

K.Y.Y. and K.J.V. conceived the experiments. K.Y.Y. and D.Y.O. performed the numerical simulations. K.Y.Y. developed the fabrication method with assistance from H.L. K.Y.Y., K.B., D.C.C., P.D., S.A.D., S.B.P. and K.J.V. designed and built the EOM comb-assisted dispersion measurement set-up. K.Y.Y., K.B., D.C.C., X.Y., P.D. and J.L. performed the dispersion measurement, and K.Y.Y., K.B., D.C.C., X.Y., P.D., J.L., S.A.D., S.B.P. and K.J.V. analysed the data. K.Y.Y. and K.J.V. prepared the manuscript with input from all co-authors.

Additional information

Supplementary information is available in the online version of the paper. Reprints and permissions information is available online at www.nature.com/reprints. Correspondence and requests for materials should be addressed to K.J.V.

Competing financial interests

The authors declare no competing financial interests.

© 2016 Macmillan Publishers Limited. All rights reserved

Methods

Device fabrication. The fabrication process was based on the method for a chemically etched wedge-resonator[37]. Disk resonators were fabricated on (100) prime-grade float-zone silicon wafers. The first SiO_2 layer was thermally grown at 1,000 °C with a thickness in the range of 7–9 μm, and the photoresist was patterned using a Karl Suss MA-6 aligner on the oxide layer. Hexamethyldisilazane (HMDS) was also deposited before the photoresist coating for wedge angles larger than 20°. For wedge angles in the range of 8°–20°, photoresist was spin-coated on the oxide layer without HMDS. The photoresist thickness was used to adjust the wedge angle. The photoresist pattern acted as an etch mask during immersion in a buffered hydrofluoric acid (HF) solution, and the resist was removed once wet etching was completed. The second SiO_2 layer was grown at the same temperature as the etched wedge disk, and the thickness of the oxide was accurately controlled via the duration of thermal oxidation. Again, the photoresist was patterned on the oxide layer and the wet etch created further wedge angles. After cleaning to remove the photoresist and residues, a XeF_2 dry etch was applied to etch the Si.

Finite element simulation. The numerical calculations were implemented using the COMSOL multiphysics package. The fibre parameters used in Fig. 1 were from refs 7, 11, and the values for the fused silica refractive index were taken from the Sellmeir equation of ref. 47. Resonator dispersion was calculated via an iterative approach[13]. Figure 1a,b use a resonator thickness of 8 μm, and Fig. 1c,d use outer wedge heights of 3 μm and 5 μm for the angle ordering 45°–10° (red) and 10°–45° (blue), respectively. Figure 3b–d use a resonator geometry obtained from the fabricated devices. The oxide thickness was measured using Filmetrics model F40 and Dektak 3ST profilometer, and the wedge profile was obtained using an atomic force microscope (Bruker Dimension ICON) and scanning electron microscope (Hitachi S-4100).

© 2016 Macmillan Publishers Limited. All rights reserved